



Topographic Guidance in Melt-Electrowritten Tubular Scaffolds Enhances Engineered Kidney Tubule Performance

OPEN ACCESS

Edited by:

Khoon Lim,
University of Otago, Christchurch,
New Zealand

Reviewed by:

Elena M. De-Juan-Pardo,
University of Western
Australia, Australia
Brooke Farrugia,
The University of Melbourne, Australia
Tim Dargaville,
Queensland University of
Technology, Australia

*Correspondence:

Miguel Castilho
M.DiasCastilho@umcutrecht.nl
Rosalinde Masereeuw
r.masereeuw@uu.nl

†These authors have contributed
equally to this work

Specialty section:

This article was submitted to
Biomaterials,
a section of the journal
Frontiers in Bioengineering and
Biotechnology

Received: 14 October 2020

Accepted: 16 December 2020

Published: 18 January 2021

Citation:

van Genderen AM, Jansen K,
Kristen M, van Duijn J, Li Y,
Schuurmans CCL, Malda J,
Vermonden T, Jansen J, Masereeuw R
and Castilho M (2021) Topographic
Guidance in Melt-Electrowritten
Tubular Scaffolds Enhances
Engineered Kidney Tubule
Performance.
Front. Bioeng. Biotechnol. 8:617364.
doi: 10.3389/fbioe.2020.617364

Anne Metje van Genderen^{1†}, Katja Jansen^{1†}, Marleen Kristen^{1,2}, Joost van Duijn^{2,3},
Yang Li^{2,3}, Carl C. L. Schuurmans^{1,4}, Jos Malda^{2,3,5}, Tina Vermonden^{3,4}, Jitske Jansen⁶,
Rosalinde Masereeuw^{1,3*} and Miguel Castilho^{2,3,7*}

¹ Division of Pharmacology, Utrecht Institute for Pharmaceutical Sciences, Utrecht University, Utrecht, Netherlands,

² Department of Orthopaedics, University Medical Center Utrecht, Utrecht University, Utrecht, Netherlands, ³ Regenerative
Medicine Center Utrecht, University Medical Center Utrecht, Utrecht, Netherlands, ⁴ Division of Pharmaceutics, Utrecht
Institute for Pharmaceutical Sciences, Utrecht University, Utrecht, Netherlands, ⁵ Department of Clinical Sciences, Faculty of
Veterinary Medicine, Utrecht University, Utrecht, Netherlands, ⁶ Department of Pathology and Pediatric Nephrology, Radboud
University Medical Center, Radboud Institute for Molecular Life Sciences, Nijmegen, Netherlands, ⁷ Department of Biomedical
Engineering, Eindhoven University of Technology, Eindhoven, Netherlands

Introduction: To date, tubular tissue engineering relies on large, non-porous tubular scaffolds ($\varnothing > 2$ mm) for mechanical self-support, or smaller ($\varnothing 150\text{--}500\ \mu\text{m}$) tubes within bulk hydrogels for studying renal transport phenomena. To advance the engineering of kidney tubules for future implantation, constructs should be both self-supportive and yet small-sized and highly porous. Here, we hypothesize that the fabrication of small-sized porous tubular scaffolds with a highly organized fibrous microstructure by means of melt-electrowriting (MEW) allows the development of self-supported kidney proximal tubules with enhanced properties.

Materials and Methods: A custom-built melt-electrowriting (MEW) device was used to fabricate tubular fibrous scaffolds with small diameter sizes ($\varnothing = 0.5, 1, 3$ mm) and well-defined, porous microarchitectures (rhombus, square, and random). Human umbilical vein endothelial cells (HUVEC) and human conditionally immortalized proximal tubular epithelial cells (ciPTEC) were seeded into the tubular scaffolds and tested for monolayer formation, integrity, and organization, as well as for extracellular matrix (ECM) production and renal transport functionality.

Results: Tubular fibrous scaffolds were successfully manufactured by fine control of MEW instrument parameters. A minimum inner diameter of 1 mm and pore sizes of 0.2 mm were achieved and used for subsequent cell experiments. While HUVEC were unable to bridge the pores, ciPTEC formed tight monolayers in all scaffold microarchitectures tested. Well-defined rhombus-shaped pores outperformed and facilitated unidirectional cell orientation, increased collagen type IV deposition, and expression of the renal transporters and differentiation markers organic cation transporter 2 (OCT2) and P-glycoprotein (P-gp).

Discussion and Conclusion: Here, we present smaller diameter engineered kidney tubules with microgeometry-directed cell functionality. Due to the well-organized tubular fiber scaffold microstructure, the tubes are mechanically self-supported, and the self-produced ECM constitutes the only barrier between the inner and outer compartment, facilitating rapid and active solute transport.

Keywords: tissue engineering, melt-electrowriting, bioartificial kidney, contact guidance, 3D culture

INTRODUCTION

In vivo, cells are surrounded by an extracellular matrix (ECM), a three-dimensional network composed of collagen, glycoproteins, polysaccharides, and other macromolecules (van Genderen et al., 2018). Underneath epithelial and endothelial cells, including renal proximal tubules and peritubular vasculature, the ECM is formed as a thin, highly specialized basement membrane (BM), which acts both as supporting scaffold for the cells, and as barrier between an inner and outer compartment (van Genderen et al., 2018). For kidney tubule engineering, a big challenge is the creation of renal proximal tubules in close proximity to peritubular vasculature. To allow for rapid exchange of solutes between blood and urine, the epithelial and endothelial BM should be virtually the only barriers between both cell types. To date, tubular tissue engineering mostly relies on non-porous, large diameter tubular scaffolds ($\varnothing > 2$ mm) for sufficient self-support, or smaller tubular lumens ($\varnothing < 1$ mm) surrounded by hydrogels to account for physiological functions, including vectorial transport (Homan et al., 2016; Jansen et al., 2017; Rayner et al., 2018; Lin et al., 2019; Singh et al., 2020). The latter has been addressed recently in valuable *in vitro* tools for drug screening and disease modeling, with proven apical-basal cell polarity, and active reabsorption and transepithelial secretion function. These models provided evidence for the fact that tubular 3D curvature and biomimetic ECM properties enhance kidney cell functionality (Jansen et al., 2015, 2016; Homan et al., 2016; Rayner et al., 2018; Lin et al., 2019; Singh et al., 2020). However, for the engineering of potentially implantable and durable kidney tubules, scaffolds must meet at least three criteria: they must be (1) small-sized and highly porous to increase the surface area, (2) freely accessible from the basolateral and luminal sides for rapid solute exchange and removal, and (3) flexible and yet strong enough to withstand intracorporeal forces such as pressure, tear and wear. Ideally, scaffolds for tubular tissue should also be resorbable and initially provide biophysical instructions to promote cell growth, differentiation, and BM production.

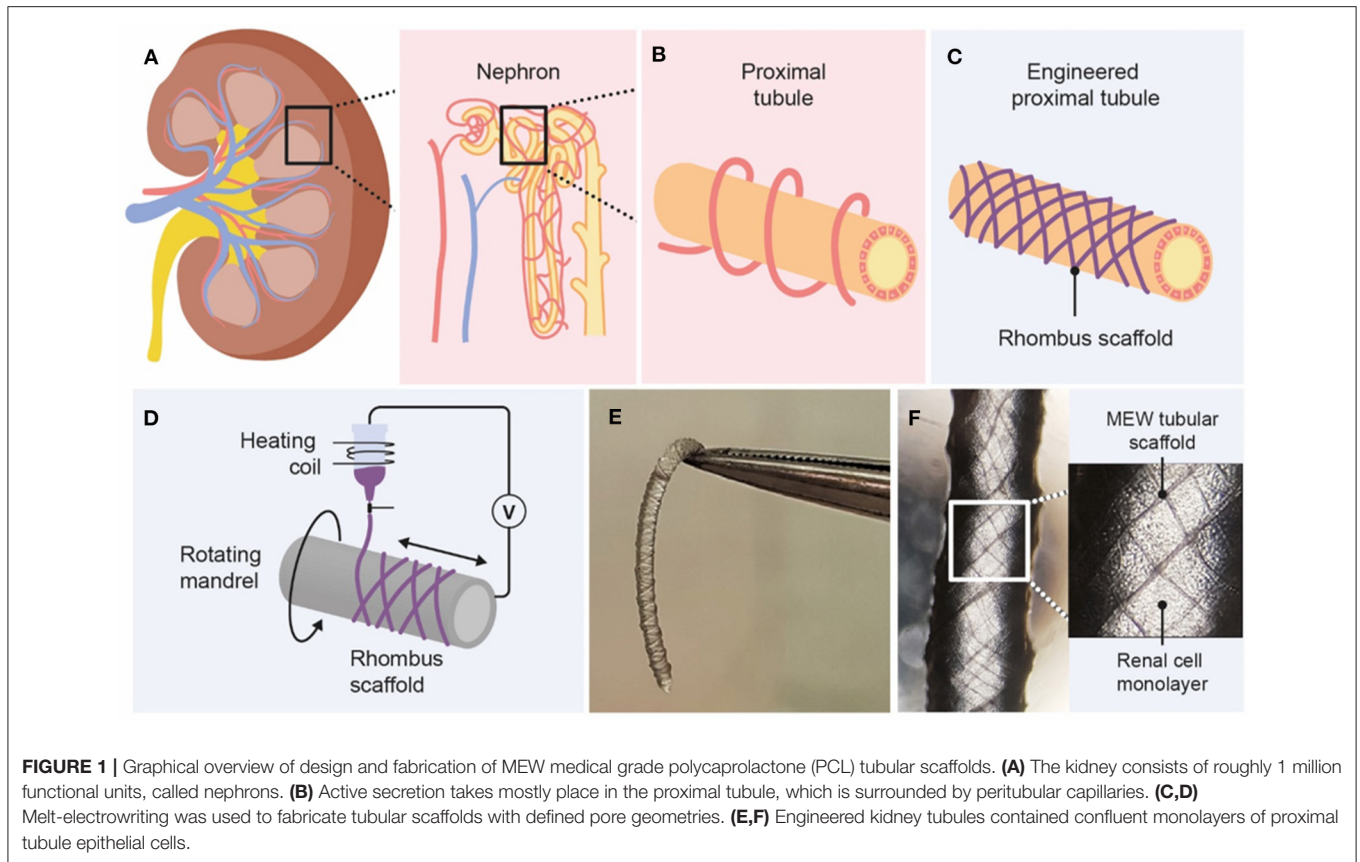
Fibrous scaffold meshes, alone or as reinforcement of hydrogels, can greatly improve the mechanical properties of engineered tissue. At the same time, they can influence cellular functionality and ECM deposition through proper scaffold design. Fibrous scaffolds have shown to facilitate cell migration and functionality by providing physiologically relevant mechanical stimulation (Castilho et al., 2017, 2019; Jansen et al., 2019). For instance, cell growth and growth directionality can be positively affected by microfibers when ordered along a preferential direction (Castilho et al., 2017; Kennedy et al., 2017).

Previously, we provided proof-of-concept for stand-alone $\varnothing < 1$ mm kidney tubule grafts fabricated by solution electrospinning (SES), in which human kidney cells were able to bridge considerable fiber-to-fiber distances without the need of embedding hydrogels, which ensured rapid solute uptake (Jansen et al., 2019). Although SES was successful on manufacturing porous tubular fiber scaffolds, this process was rather limited by poor patterning control and hence fabrication reproducibility. Here, we fabricated tubular scaffolds using a superior electrohydrodynamic fiber printing technique called melt electrowriting (MEW) (Brown et al., 2011, 2014). MEW is a solvent-free technique that involves extrusion of a molten polymer fiber onto a computer-controlled collector. Organized 3D tubular constructs are obtained by precise fiber deposition on a rotating cylinder and successive layer-by-layer stacking, which require fine control over instrument parameters, in particular mandrel rotation and translation velocity (Brown et al., 2011; McColl et al., 2018; Robinson et al., 2019). Using MEW, we report the successful fabrication of $\varnothing < 1$ mm proximal tubule units that meet all above-mentioned criteria (**Figure 1**). The first aim was to determine optimal fabrication parameters for $\varnothing = 0.5$ mm and 1 mm tubular scaffolds and to assess their mechanical characteristics. The second aim was to apply these scaffolds to renal epithelial and vascular tubule engineering using conditionally immortalized proximal tubule epithelial cells (ciPTEC) and human umbilical vein endothelial cells (HUVEC); however, only renal epithelial cells were able to form monolayers within the scaffold pores and were used for subsequent experiments. Positive effects of tube structure and biomimetic materials on renal function have already been proven in literature; here, we hypothesized that by engineering tubular scaffolds with defined pore microarchitecture (i.e., rhombus, square and random), we can provide adequate topographic cues to promote cell directionality, autologous BM production, and renal transport function.

MATERIALS AND METHODS

Melt Electrowriting

We used a custom-built MEW device consisting of a rotating aluminum mandrel ($\varnothing = 3, 1, 0.5$ mm) mounted on a x-y axis and a custom print head mounted of a movable z-axis. The x-y-z axes were computer-controlled using an advanced motion controller MC403 (Trio Motion Technology Ltd.). Granular medical grade polycaprolactone (PCL, Purasorb PC 12, Corbion) was loaded into a 3 ml electrically heated glass syringe with a 27G size metallic nozzle and molten for 30 min prior printing. The molten



polymer was electrified using a high voltage source (Heinzinger, LNC 30000-5 POS, 0–30 kV), and extrusion was assisted by a high-resolution air pressure regulator (VPPE-3-1-1/8-2-010-E1, Festo). In order to control scaffold microarchitectures, the effect of tangential rotation velocity (V_{tang}) and translation velocity (V_{trans}) on the laydown fiber winding angle (α) was investigated (**Supplementary Figure 1**). The theoretical winding angle was determined according to,

$$\alpha = \text{ArcTang}(V_{\text{tang}}/V_{\text{trans}}) \quad (1)$$

for $0 < \alpha < 90^\circ$. The V_{tang} expressed in mm/s was assessed by,

$$V_{\text{tang}} = \pi d V_r \quad (2)$$

where d is the diameter of the collecting mandrel in mm and V_r is the rotational velocity of the mandrel in rad/s. Both V_{tang} and V_{trans} were varied according to specified in **Table 1** in order to obtain scaffolds with winding angles of 30 and 45°, corresponding to a square and rhombus microarchitecture, respectively; and a densely distributed crossed fibremat (alternating winding angles between 30, 45, and 60°) here named random. The x-y position of the mandrel and respective translational velocity were programmed using a commercially available software package (Motion Perfect V4.2, Trio Motion Technology Ltd.) while the rotational velocity was controlled by Arduino IDE software. The combination

of parameters used to obtain the three different scaffold microgeometries and tubular diameters is summarized in **Table 1**. After fabrication, the mandrel with the printed tubular scaffold was soaked in ethanol for 5 min to facilitate scaffold removal. As the 0.5 mm mandrels showed some variation of working distance between the mandrel and the nozzle, 1 mm tubes were used for the biological experiments.

Imaging and Structural Characterization

Tubular scaffolds microstructure and fiber size were analyzed by stereomicroscopy (Olympus SZ61) and by scanning electron microscopy (SEM, Phenom Pro, Phenom-World). SEM was performed at an acceleration speed of 5–10 kV. Prior imaging, SEM scaffolds were gold sputtered coated (1 nm) using a Q150R rotary-pumped sputter (Quorum Technologies). Images from both stereomicroscope and SEM were analyzed with Image J (National Instruments). Scaffold porosity was determined gravimetrically.

Cell Culture

Human conditionally immortalized proximal tubule epithelial cells (ciPTEC), isolated from human kidney tissue, were developed by Jansen et al. (2014). The tissue used for cell line development was obtained from non-transplanted donors with given informed consent. Briefly, proximal tubule cells obtained from healthy volunteers were infected with a temperature sensitive mutant U19tsA58 of SV40 large T antigen (SV40T) and

TABLE 1 | Summary of printing parameters used to fabricate melt-electrowritten tubular scaffolds.

Winding angle (°)	Tube diameter (mm)	Effective speed (mm/s)	Tangential speed, Vtang (mm/s)	Translational speed, Vtrans (mm/s)	High voltage (kV)	Melting temperature (°C)	Dispensing pressure	Collecting distance (mm)
30	0.5	3	1.5	2.6	6.5	90	0.65	4
	1	3	1.5	2.6	5.5	85	1	4
	3	3	1.5	2.6	5.0	80	1	4
45	0.5	3	2.1	2.1	6.5	90	0.65	4
	1	3	2.1	2.1	5.5	85	1	4
	3	3	2.1	2.1	5.0	80	1	4
60	0.5	3	2.6	1.5	6.5	90	0.65	4
	1	3	2.6	1.5	5.5	85	1	4
	3	3	2.6	1.5	5.0	80	1	4

the essential catalytic subunit of human telomerase (hTERT). ciPTEC were cultured at 33°C and 5% (v/v) CO₂ up to 90% confluency to maintain a cell proliferation state. For maturation, ciPTEC were transferred to 37°C for at least 7 days prior to experimental readout. ciPTEC were cultured in T175 cultures flasks (Greiner Bio-One), using Dulbecco's modified eagle medium/HAM's F12 without phenol red (ThermoFisher Scientific), supplemented with 5 µg mL⁻¹ insulin, 5 µg mL⁻¹ transferrin, 5 µg mL⁻¹ selenium, 35 ng mL⁻¹ hydrocortisone, 10 ng mL⁻¹ epidermal growth factor, 40 pg mL⁻¹ tri-iodothyronine (Sigma-Aldrich), 10% fetal bovine serum (FBS) (Greiner Bio-One), and 1% penicillin/streptomycin (ThermoFisher Scientific). For 2D cultures, ciPTEC were cultured and matured in 6 well plates. Primary human umbilical vein endothelial cells (HUVEC) [American Type Culture Collection (ATCC)] were cultured using vascular cell basal medium and endothelial cell growth kit-VEGF (ATCC). HUVEC were cultured in T175 culture flasks (Greiner Bio-One) at 37°C and 5% (v/v) CO₂, and confluency was maintained at a maximum of 90% throughout the culture period.

Scaffold Coating and Cell Seeding Onto Scaffolds

Before cell seeding, PCL tubular scaffolds were sterilized using 70% ethanol evaporation and UV exposure (365 nm for 15 min). 2 mg/mL L-3,4- dihydroxyphenylalanine (L-DOPA, Sigma-Aldrich) was dissolved in 10 mM tris(hydroxyethyl)aminomethane (Tris) pH 8.5 buffer at 37°C for 45 min (Ni et al., 2011; Oo et al., 2011; Jansen et al., 2015). After sterile filtration (0.2 µm pore size), scaffolds were coated through submersion for 4 h at 37°C and thoroughly washed with phosphate buffered saline (PBS without calcium and magnesium, Lonza). Next, 10 × 10⁶ cells/ml were added in small culture medium drops onto flat scaffolds or injected into tubular scaffolds. Cells were incubated for 4 h at 33°C (ciPTEC) or 37°C (HUVEC); tubular scaffolds were turned 180° after 2 h. Afterwards, culture medium was added, and the constructs were cultured until confluency at 33°C and then at 37°C (ciPTEC), or directly at 37°C (HUVEC). Scaffolds were cultured for 1–4 weeks at 37°C. Culture medium was refreshed 3x per week. Changes on polymer surface wettability before and

after L-DOPA coating were evaluated by static contact angle measurements using sessile drop technique (Data Physics, OCA 15EC). Measurements were performed according to a procedure described elsewhere (Castilho et al., 2017).

Immunofluorescence

Scaffolds were fixed for 5 min with 4% (v/v) paraformaldehyde in PBS and permeabilized with 0.3% (v/v) triton X-100 in PBS for 10 min at RT. Subsequently, cells were exposed to blocking buffer consisting of 2% (v/v) FCS, 0.5% (w/v) bovine serum albumin (BSA), and 0.1% (v/v) Tween20 in PBS for 30 min at RT. Antibodies were diluted in blocking buffer. Primary antibodies were incubated O/N at 4°C and secondary antibodies for 1 h at RT. We used the following primary and secondary antibodies and dilutions: mouse monoclonal anti-α-tubulin 1:150 (T6793, Sigma-Aldrich), goat monoclonal anti-collagen IV 1:50 (1340-01, Southern Biotech), and mouse monoclonal anti CD31 1:250 (ab119339, Abcam), AlexaFluor 488 donkey-anti-rabbit 1:200 (Invitrogen), AlexaFluor 488 goat-anti-mouse 1:200 (Invitrogen), and AlexaFluor 647 donkey-anti-goat 1:200 (Invitrogen). Moreover, we used AlexaFluor 546 phalloidin 1:1,000 (A22283, Thermo Fisher Scientific) to stain actin filaments, and nuclei were stained using DAPI 1:1,000 (Sigma-Aldrich). Immunofluorescence was examined using confocal microscopy (Leica TCS SP8 X) and software Leica Application Suite X. Images were analyzed using ImageJ. Images were converted to 8-bit, Z-projections were made, and the same threshold was applied for every image. Actin filament directionality was quantified using the directionality functionality and Fourier components analysis.

Gene Expression

Gene expression analysis was performed by RT-qPCR on ciPTEC after growing at 33°C until confluency and 7 days at 37°C. RNA was isolated from ciPTEC grown in tubular scaffolds or in L-Dopa coated well plates (control) using a PureLink RNA mini kit (Invitrogen), and cDNA was prepared using 500 ng sample RNA templates using iScript¹ cDNA Synthesis Kit (BioRad). RT-qPCR analysis was performed on a CFX96 real-time PCR detection system (BioRad) using TaqMan Universal PCR Master

¹RNA isolation kit that was used for this protocol.

Mix and TaqMan Gene Expression Assay (Thermo Fisher Scientific) for *COL4A1* (TaqMan Assay ID: Hs00266237_m1), *ABCG2* (Hs01053790_m1), *ABCC4* (Hs00988721_m1), *ABCB1* (Hs00184500_m1) and *SLC22A2* (Hs00533912_m1), *RPS18* (Hs01375212_g1). All reactions were carried out with equivalent dilutions of each cDNA sample.

Mechanical Testing

The mechanical properties of cell free and cell cultured tubular constructs (day 14 of culture at 37°C) were studied under uniaxial tensile test using a Dynamic Mechanical Analyzer (DMA Q800, TA Instruments). Before testing, cell cultured constructs were washed with HBSS, fixated for 10 min with 4% (v/v) paraformaldehyde and then washed again with HBSS. Tensile tests were performed at a rate of 0.1 N/min. Prior testing, nominal diameter and length of each construct was measured using stereomicroscopic and SEM images. The tangent modulus, yield strain and elastic strain energy were determined from engineered stress-strain curves. Tangent moduli were determined using a least square fit of the initial slope of the stress-strain elastic region (E_T , as presented in **Supplementary Figure 3**), yield point (ϵ_{el}) was defined as point where nonlinear deformation begins and elastic strain energy (U_0) was obtained,

$$U_0 = \int_0^{\epsilon_{el}} \sigma d\epsilon \quad (3)$$

where σ and ϵ represent engineered stress and strain, respectively.

Functional Assays

To test the functionality of various transporters (BCRP, MRP4, P-gp and OCT2), tubular scaffolds with rhombus-shaped pores and ciPTEC were matured for 3 weeks, rinsed in HBSS, and incubated with fluorescent substrates. Cells were incubated with 1 μ M non-fluorescent calcein-AM for 15 min at 37°C to confirm cellular metabolism through enzymatic conversion of calcein-AM to fluorescent calcein. Incubation was performed in presence or absence of 5 μ M MK-571 and KO173 (inhibitors of MRP4 and BCRP) to validate functional excretion of calcein. Moreover, tubular scaffolds were incubated with 10 μ M rhodamine123 (RH123), substrate for uptake transporter OCT2 and excretion transporter P-gp, in presence or absence of 5 μ M tetrapentylammonium (TPA⁺, OCT2 inhibitor) or 5 μ M PSC-833 (P-gp inhibitor) for 40 min at 37°C. After incubation, the scaffolds were rinsed with HBSS and images were captured with green filters using the Keyence BZ-9000 fluorescence microscope (Keyence). ImageJ (National Instruments) was used to measure fluorescence intensity in 16-bit images after background subtraction. In addition, a leakage assay was performed with rhombus-shaped scaffolds to assess engineered proximal tubule function. First, a customized perfusion chamber was designed and printed with polylactic acid (PLA) using a fused filament fabrication method (Ultimaker). The printed chamber was mounted on a glass slide using epoxy glue (Loctite), and tubular scaffolds were fixed inside with dental glue (GI-MASK Automix, Coltene) (**Supplementary Figure 4**). Scaffolds were perfused with 0.1 mg/ml fluorescein isothiocyanate-inulin for

5 min (inulin-FITC, Sigma-Aldrich), and real-time imaged using a fluorescence microscope with a green filter (Keyence BZ-9000).

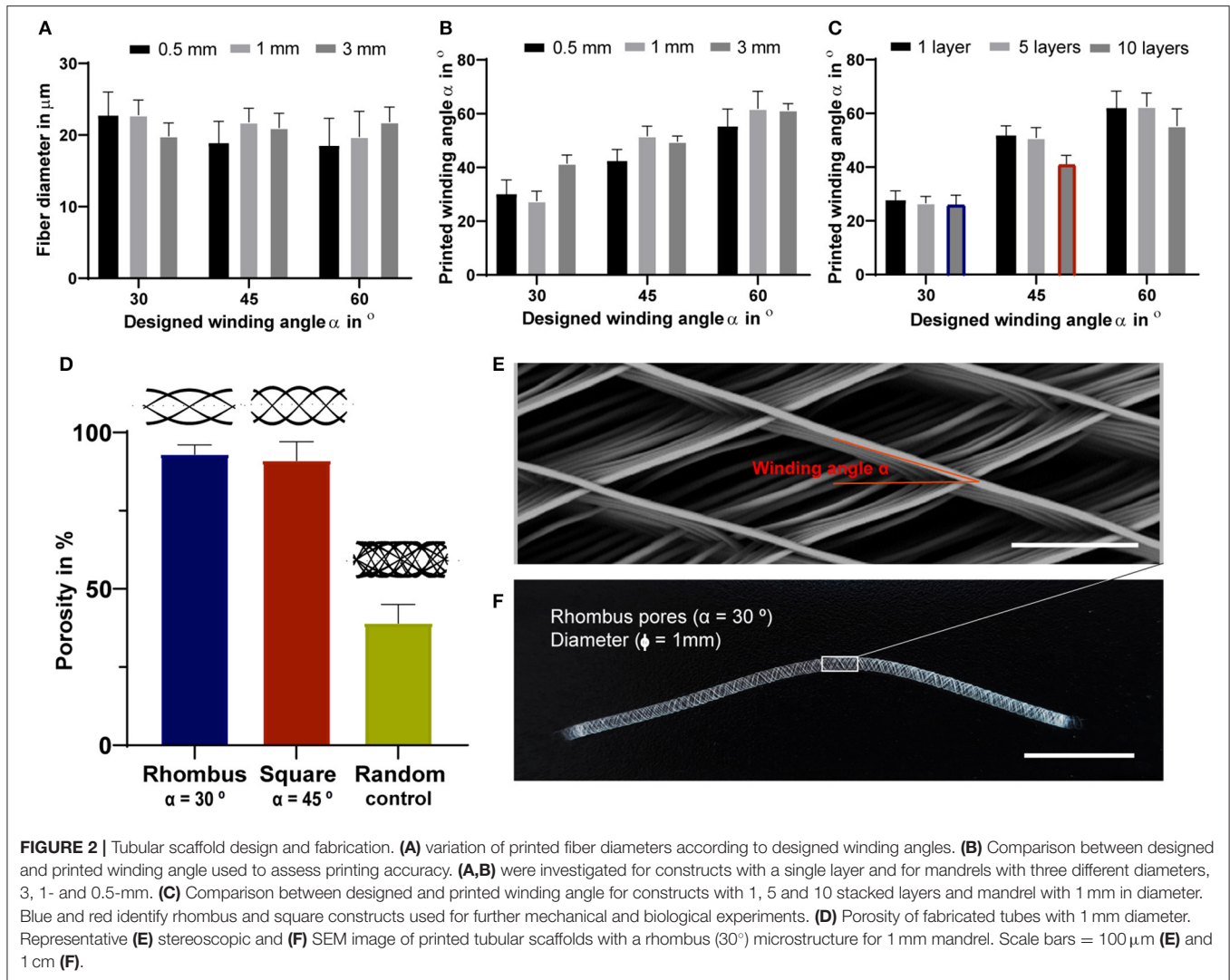
Statistical Analysis

Unless otherwise stated, 3 scaffolds per condition were used in 3 independent experiments respectively. Statistical analysis was carried out in Graphpad Prism 8.1.0 (GraphPad Software Inc.) using a student *t*-test when two groups were compared, and a one-way ANOVA and Tukey's multiple comparisons *post-hoc* test when 3 or more groups were compared. A two-way ANOVA and multiple comparisons were used for comparison of multiple groups with 2 independent variables. Differences were considered significant with a *p*-value of $p < 0.05$. * indicates $p < 0.05$, ** $p < 0.01$, *** $p < 0.001$ and **** $p < 0.0001$. Data are represented as mean \pm standard error of the mean (SEM) or as mean \pm standard deviation (SD).

RESULTS

Design and Fabrication of Microfibrous Tubular Scaffolds

Fully resorbable medical grade polycaprolactone (PCL) tubular scaffolds were manufactured with a reproducible quality using an in-house built MEW set-up (**Figures 1, 2, Supplementary Movie 1**). Scaffolds were fabricated with a range of winding angles, from 30° to 60°, by controlling the ratio between the tangential rotation velocity (V_{tang}) and the translation velocity (V_{trans}) (**Supplementary Figure 1**). No significant differences in fiber diameter were observed when varying the winding angle (constant fiber diameter of approximately 20 μ m, **Figure 2A**), and the measured winding angle was in accordance with the theoretical design (**Figure 2B**). Additionally, the effect of fiber stacking on printed winding angle was evaluated (**Figure 2C, Supplementary Figure 2**). In general, an increase in the deviation between designed and printed winding angle was observed when increasing the number of staked fibers from 1 to 10 layers. This difference was in average 33 ± 8 for 0.5 mm mandrels (**Supplementary Figure 2A**) and $7 \pm 3\%$ for 3 mm (**Supplementary Figure 2B**) and 1 mm mandrels (**Figure 2C**). Importantly, our results demonstrate that the fiber diameter did not change significantly when increasing the number of staked layers, as well as when varying the winding angle. Furthermore, while 3 and 1 mm diameter tubes could be easily removed from the mandrels, harder removal of 0.5 mm tubes from the mandrel was observed, which compromised their structural integrity. Based on these post-processing handling characteristics and printing fidelity results, tubes with 1 mm diameter and 10 layers (final thickness of $\sim 100 \mu$ m) were selected for further experiments. Tubular scaffold with three different microarchitectures were fabricated, i.e., rhombus (winding angle 30°), square (winding angle 45°) and random (densely distributed crossed fiber mat, with winding angles varying between 30, 45, and 60°). Notably, interconnected porosities above 90% and controlled pore sizes of 200 μ m were obtained for rhombus (**Figures 2D–F**) and square pore shaped scaffolds, while only 40% porosity were observed for random scaffolds and no controlled pore size (**Figure 2D**).

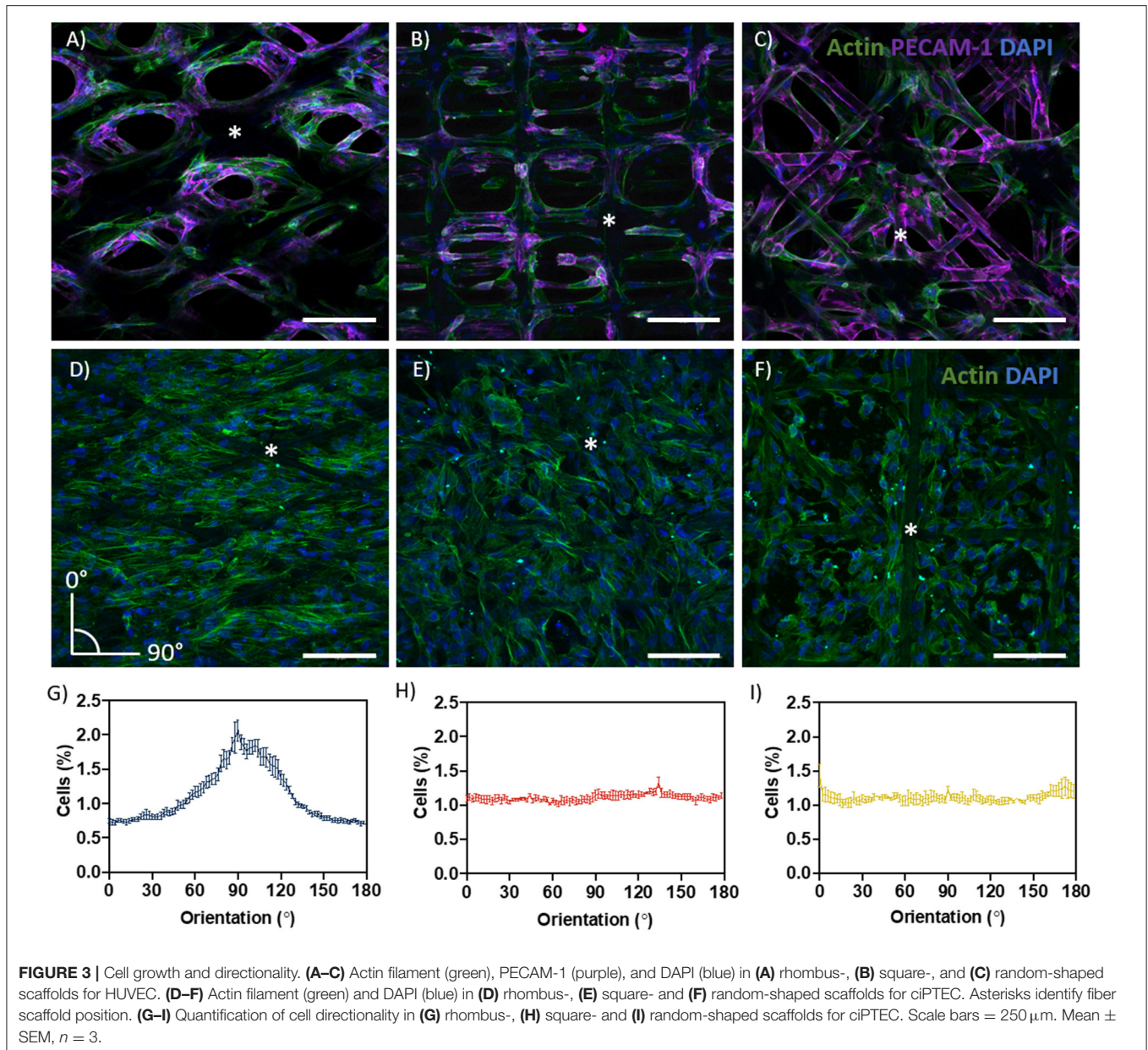


Cell Growth and Directionality

The first requirement of functional bioengineered kidney tubules is cell adherence and growth into a barrier-forming monolayer. Confirming our previous data, ciPTEC were able to form tight monolayers in L-DOPA biofunctionalized tubular scaffolds by stretching across the pores between the PCL microfibers (Jansen et al., 2019). L-DOPA coating increased scaffold hydrophilicity compared to non-coated tubular scaffolds (**Supplementary Table 1**). Cells grew on the PCL-fibers, then they started bridging the pores from the corners and moved further inward; ultimately, the pores were entirely filled by ciPTEC monolayers. Only at a pore size of 400 μm and higher, ciPTEC were not able to bridge the gap.

Cell growth and filamentous actin (F-actin) orientation were studied in scaffolds with rhombus, square and random pore geometries (**Figures 3A–I**). For HUVEC, no microgeometry allowed monolayer formation; the cells only surrounded the PCL fibers (**Figures 3A–C**). When stained for platelet endothelial

cell adhesion molecule 1 (PECAM-1 or CD31), a marker for endothelial cell junctional integrity, we observed irregular expression (**Figures 3A–C**). PECAM-1 is only expressed at the cell borders of confluent monolayers, whereas little or no expression is observed in sparse or migrating endothelial cells (RayChaudhury et al., 2001; Privratsky and Newman, 2014). In contrast to HUVEC, ciPTEC were able to fill the pores with all geometries investigated. For ciPTEC, rhombus-shaped pores caused preferential cell alignment along the scaffold fiber direction. The angle of deviation for ciPTEC grown in rhombus-shaped pores was approximately 25°, which is in accordance with the 30° winding angle of the pores, indicating that ciPTEC are aligned as instructed by the geometry. The cell alignment order parameter S was calculated for ciPTEC, where a value of $S = 1$ would indicate that the long axis of the cells perfectly aligned with the scaffold fiber direction and $S = 0$ indicated no particular cell alignment. CiPTEC grown on rhombus-shaped pores exhibited cell alignment with an S of 0.51 ± 0.06 , whereas both square and random microgeometries resulted in an isotropic distribution of



cells with order parameters of 0 (**Figures 3D–I**) (Duclos et al., 2014; Li et al., 2017).

Renal Transporter Expression and Function

The proximal tubule has a major role in waste secretion from the blood into the urine, and, therefore, expresses a broad range of functional transporters to facilitate this transport. We tested the effect of pore microgeometries on the gene expression of four relevant transporters: the efflux pumps breast cancer resistance protein (BCRP), multidrug resistance-associated protein 4 (MRP4), and P-glycoprotein (P-g), and the uptake transporter organic cation transporter 2 (OCT2). For all microgeometries, mRNA levels were compared to 2D culture (**Figures 4A–D**). For BCRP (**Figure 4A**, CT value 2D: 33.47 ± 0.12) and MRP4

(**Figure 4B**, CT value 2D: 29.60 ± 0.03), no differences were found. Remarkably, mRNA expression for P-gp increased 2.4-fold (**Figure 4C**, $p < 0.05$, CT value 2D: 29.43 ± 0.03) for tubular scaffolds with rhombus-shaped pores compared to 2D culture. Also, OCT2 expression was 3.4-fold higher (**Figure 4D**, $p < 0.01$, CT value 2D: 37.85 ± 0.30). In tubular scaffolds with isotropic pore microgeometries, transporter expression showed no significant increase compared to traditional 2D culture. Two functional assays were performed to validate transporter function in rhombus-shaped pores (**Figures 4E–J**). Calcein-AM diffuses into the cell, where it is hydrolyzed by esterases into fluorescent calcein, which is then secreted by BCRP and MRP4 (**Figure 4E**) (Caetano-Pinto et al., 2016). When incubating the engineered kidney tubules with calcein-AM in presence of BCRP and MRP4

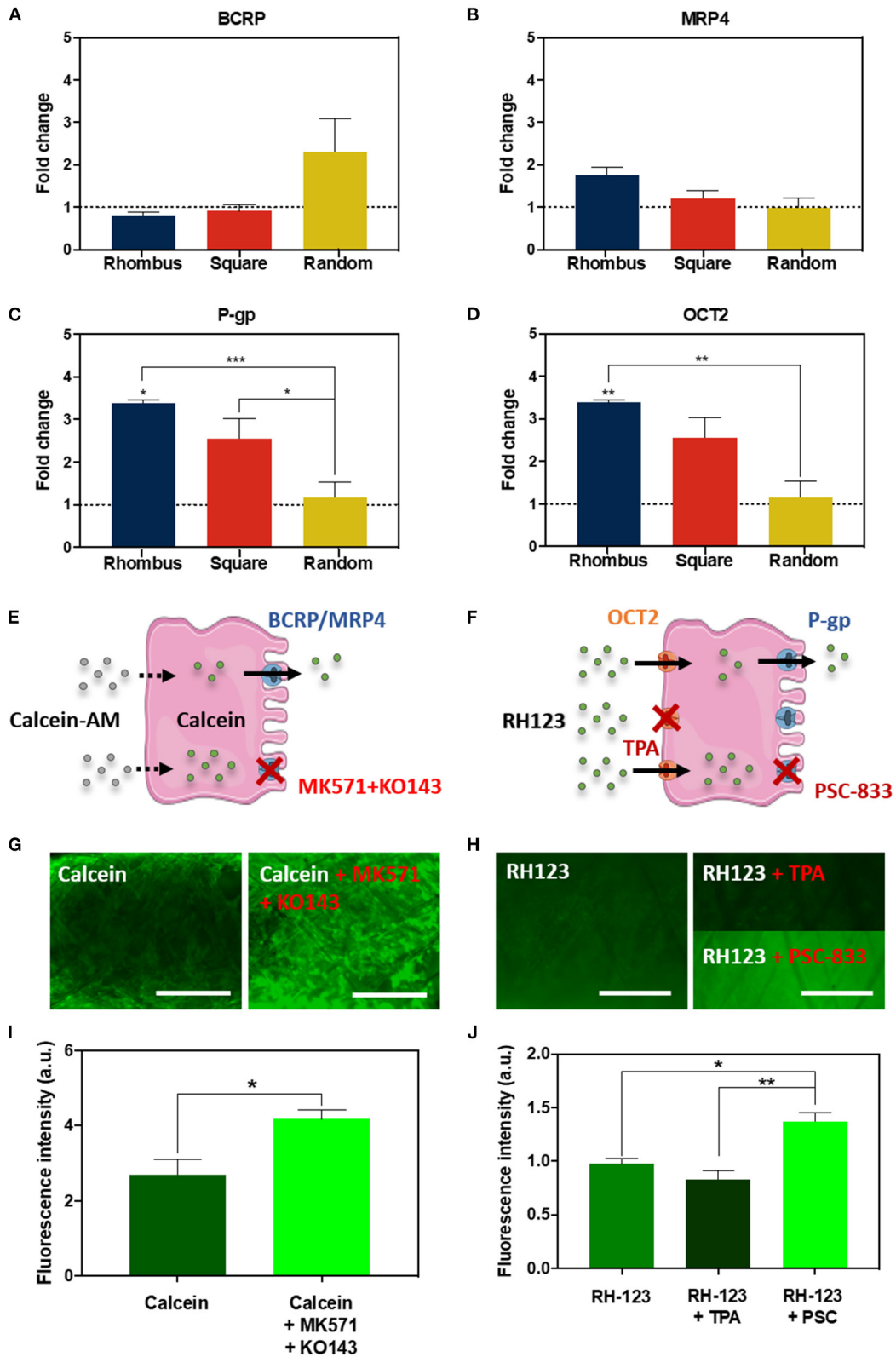
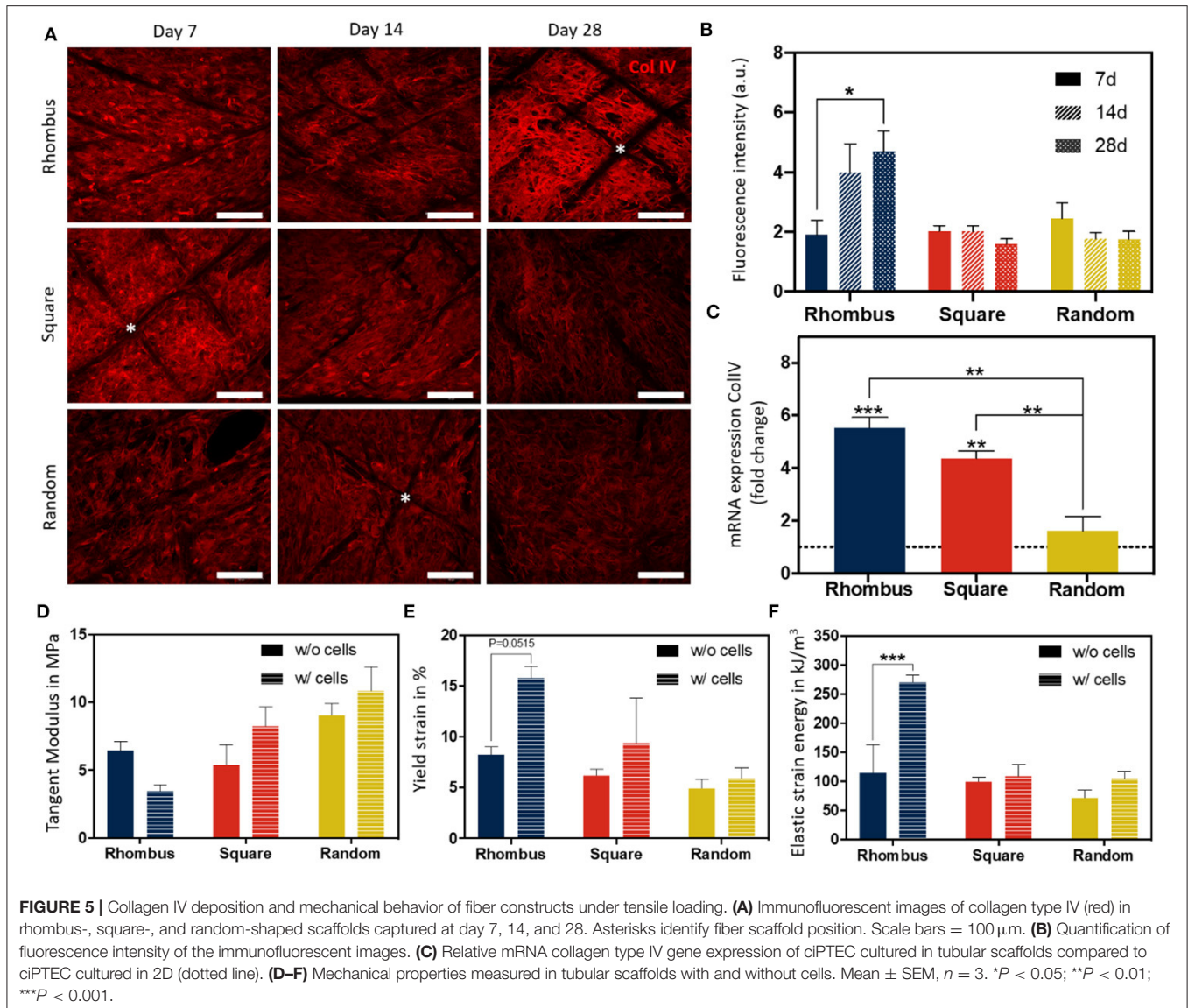


FIGURE 4 | Renal transporter expression and function. (A–D) Relative mRNA gene expression of ciPTEC cultured in tubular scaffolds with rhombus-shaped pores compared to ciPTEC cultured in 2D (dotted line). (E,F) Graphical overview of (E) calcein-AM assay and (F) rhodamine123 assay. (G,H) Immunofluorescent images of (G) calcein-AM assay and (H) rhodamine123 assay in presence or absence of inhibitors. (I,J) Quantification of immunofluorescent images measured as fluorescence intensity for (I) calcein and (J) rhodamine123. Scale bars = 500 μ m. Mean \pm SEM, $n = 3$. * $P < 0.05$; ** $P < 0.01$; *** $P < 0.001$.

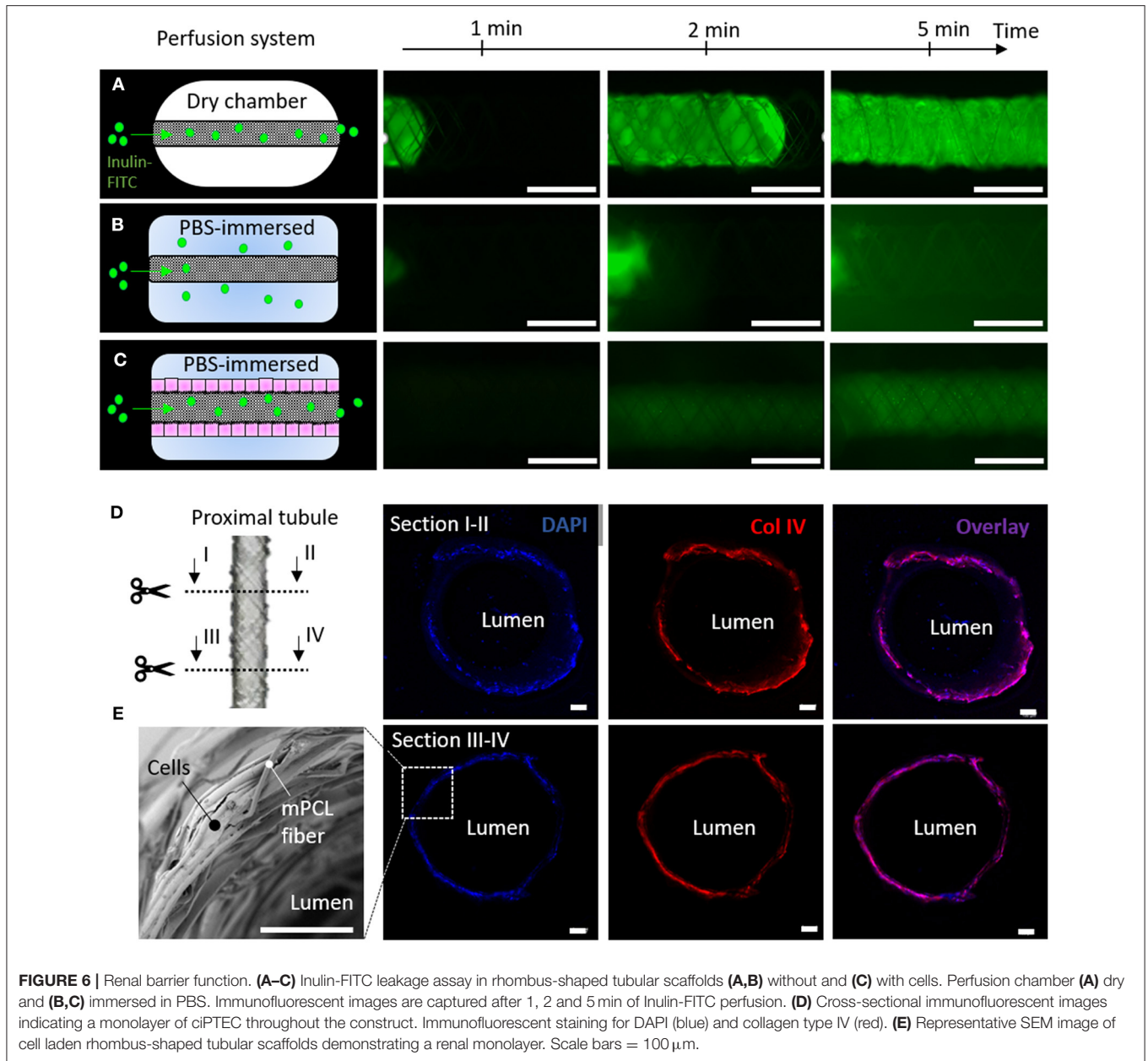


inhibitors KO143 and MK571, calcein accumulated in the cells (Figures 4G,I) ($p < 0.05$). Rhodamine-123 (RH123) is a chemical fluorescent compound that is actively transported into the cell via OCT2 and actively excreted into the urinary compartment by P-gp and BCRP (Figure 4F). When the OCT2 inhibitor TPA was added, RH123 intracellular fluorescence intensity tended to be lower, although not significantly. When the P-gp inhibitor PSC-833 was added, intracellular fluorescence intensity increased ($p < 0.05$) (Figures 4I,J).

Collagen IV Deposition

Collagen type IV is the most abundant component of the renal BM, making up 50% or more of the total (van Genderen et al., 2018). To investigate how pore microgeometries affected ECM deposition, collagen type IV expression was measured over time, i.e., at day 7, 14, and 28, after starting maturation at 37°C (Figures 5A,B). In all pore microgeometries tested, ciPTEC deposited collagen type IV and filled all pores at the earliest timepoint measured (day 7). While collagen type IV

deposition remained equal over time in random and square microgeometries, it significantly increased ($p < 0.05$) in rhombus scaffolds, with a maximum collagen type IV expression on day 28 (Figure 5B). On mRNA level, collagen type IV expression increased 5.5-fold in rhombus-shaped pores compared to traditional 2D culture at day 7 ($p < 0.001$, CT value 2D: 32.46 ± 0.33) (Figure 5C). Square-shaped pores also increased collagen IV mRNA levels in ciPTEC (4.4-fold, $p < 0.01$), whereas random-shaped pores did not have any beneficial effect compared to 2D cell culture (Figure 5C). Finally, we assessed how cells and their BM affected the mechanical properties of the MEW tubular scaffolds. Engineered kidney tubules were matured for 14 days before they were evaluated under uniaxial tensile loading to determine tangent modulus, yield strain, and elastic strain energy (Figures 5D–F, Supplementary Figure 3). A non-linear stress-strain behavior was observed for the different tested microarchitectures (Supplementary Figure 3). Interestingly, without cells scaffolds with a rhombus geometry were able to reach higher elastic deformations (2-fold higher, approximately



10% deformation) and lower tangent modulus (1.7-fold lower, 4 MPa) than scaffolds with random microstructure (Figures 5D,E, Supplementary Figure 3). No significant differences were observed on tangent modulus and elastic strain between scaffolds with a squared and random microarchitecture. In tubular scaffolds with ciPTEC monolayers, we observed a trend for an increase in yield strain ($p = 0.0515$) and an increase in elastic strain energy ($p < 0.0002$) in tubules with rhombus-shaped pores compared to scaffolds without cells (2- to 3-fold higher). It should be noted that a promising elastic behavior (shape recovery without visual permeant deformation) was observed for rhombus scaffolds after repetitive manual stretching, not observed for square and random tubular scaffolds (data not shown).

Barrier Function

In our engineered kidney tubules, cells and their self-made BM deposited within the scaffold pores formed the only barrier between the basolateral and luminal side of the tubes. A thin but tight barrier is crucial for vectorial solute transport. To functionally assess barrier formation, inulin-FITC leakage was measured using a custom-made perfusion system. When mounting cell-free scaffolds in a dry chamber, inulin-FITC remained inside the scaffold due to surface tension (Figure 6A), but when PBS was added to the chamber, inulin-FITC directly leaked out (Figure 6B). In contrast, ciPTEC-laden scaffolds kept the inulin-FITC inside the lumen, indicating that the cells and their BM functioned as a leak-tight barrier between the luminal and basolateral sides of the engineered kidney tubule

(Figure 6C). Engineered kidney tubules were also stained for collagen type IV and DAPI, and cross-sections were randomly made to confirm monolayer formation throughout the tubular construct (Figures 6D,E). For rapid solute exchange and future implantation purposes, engineered kidney tubules must be flexible, wear-resistant, small in diameter, highly porous, and freely accessible from both the basolateral and luminal side. Using MEW, we fabricated self-supported, highly ordered tubular scaffolds with controlled pore microarchitectures (i.e., rhombus and square). We were able to produce scaffolds with an inner diameter of 0.5 mm, which is around 7 times the diameter of native kidney tubules and only 2 times the diameter of common dialysis fibers. While smaller diameters might be possible in future, the constructs also needed to remain easy to handle for experimental testing. The ability to control tubular scaffold microarchitecture is a unique characteristic of MEW that distinguishes the process from other conventional fiber formation technologies like SES. For kidney tubule engineering, we identified rhombus-shaped pores as a superior microgeometry over square- and random-shaped pores: topographic guidance resulted in directed cell growth, enhanced collagen type IV deposition, remarkably improved yield strain and elastic strain energy, and increased functional OCT2 and P-gp expression.

DISCUSSION

Rhombus-Shaped Pores Mimic *in vivo* Renal Tubular Basement Membrane Anisotropy Through Topographic Guidance

In vivo, the renal tubular BM exhibits an anisotropic structure, i.e., a directional preference in form of a polygonal meshwork of corrugated appearance (Hironaka et al., 1993). In contrast to square- and random-shaped pores, rhombus-shaped pores guided cell growth along the scaffold fibers into a preferred cell direction with an angle of deviation that was even smaller than the winding angle of the scaffold. This phenomenon is called contact or topographic guidance (Bourget et al., 2013; Andalib et al., 2016). The effects of various topographic features on ciPTEC have been evaluated previously; already small features (<5 μm) could induce cell organization and alignment, which made the cells more susceptible to mechanical cues such as fluid shear stress (FSS) (Frohlich et al., 2012, 2013; Hulshof et al., 2018). The alignment of the actin cytoskeleton might have contributed to the increased BM and transporter gene expression. Importantly, the cytoskeleton reorganization is known to alter force-activated pathways, as well as nuclear actin structures that can regulate gene expression and cell differentiation (Tremblay et al., 2013; Sankaran et al., 2019). Although more research is needed to confirm such underlying mechanisms in renal cells, our data do confirm beneficial effects of anisotropic cues on cell growth behavior and differentiation. The effects of different pore sizes and shapes of MEW scaffolds on cell alignment and gene expression have been shown to vary per cell type, including macrophages, bone marrow, smooth muscle cells, cardiomyocytes, and skeletal stem cells (Castilho et al., 2018; Eichholz and Hoey, 2018; Brennan et al., 2019; Saidy et al., 2019;

Tylek et al., 2020). This indicates that the choice of pore size and shape need to be carefully considered depending on cell type of interest. For HUVEC, it has been shown that topographic cues of ridges and grooves can stabilize the endothelial phenotype. Based on the physiological BM microarchitecture *in vivo*, alignment in circumferential direction would be preferred (Gasiorowski et al., 2010; Bourget et al., 2013). In our study, HUVEC failed in filling the MEW-fabricated pores of any microgeometry tested. Most likely, HUVEC have a smaller spreading length compared to ciPTEC, which is the only parameter besides initial pore size needed for predictions of void filling (Joly et al., 2013).

Renal Monolayers in MEW Pores Are Freely Accessible for Solute Uptake and Separate Compartments

Inhibitor-sensitive cellular uptake and excretion of fluorescent compounds demonstrated functional transport activity of our engineered kidney tubules. Vectorial solute transport requires an intact and polarized epithelial monolayer that forms a barrier between the luminal and the outer compartment. Microscopic images revealed consistent monolayer formation throughout the construct, which was confirmed by retainment of inulin-FITC during luminal perfusion. For uptake and subsequent drainage of metabolic waste products, an outside-oriented basolateral side, and an apical membrane facing the lumen are crucial. Usually, the interaction between cells and ECM are a determinant factor in the orientation and stabilization of cell polarity (Chambard et al., 1981). However, freshly seeded cells are not provided with a pre-existent ECM in our scaffolds, thus polarization likely depends on factors other than ECM cues. It is known that fluid shear stress (FSS) can facilitate cell polarization and has moreover been shown to enhance transporter expression in epithelial cells (Jang et al., 2013; Homan et al., 2016; Weber et al., 2016; Vriend et al., 2020). Possibly, FSS could induce polarization and further enhance cellular functionality in our scaffolds, therefore future steps will include the establishment of a long-term flow-compatible cell culture system.

Rhombus-Shaped Pores Increase Yield and Elastic Strain Energy of Engineered Kidney Tubules

When handled or potentially implanted, engineered kidney tubules should be able to withstand external influences like pressure, tear and friction. When subjected to axial forces, controlled pore microgeometries themselves had a significant effect on tangent modulus, yield strain and elastic energy of tubular scaffolds when compared with non-controlled pore microgeometries. This evidence was even more pronounced when cells formed monolayers within the pores. Kidney tubules with rhombus-shaped pores could sustain higher strain (~15%) before yielding compared to random and square (<10%), probably due to the contact guided cell alignment with the fiber direction. Compared to tangent moduli of kidney tissue reported in literature (3–10 MPa), the tangent modulus of 4 MPa for the kidney tubules with rhombus-shaped pores (evaluated 14 days after monolayer formation) was close to the lower limit of this range (van Genderen et al., 2018). It should be noted

that mechanical properties were tested after fixation, which tends to increase the tangent modulus (Ling et al., 2016; Kim et al., 2017). However, considering the increase in ECM deposition over the course of 28 days in culture, an overall improvement in mechanical properties can be expected over time. Notably, the control over scaffold microarchitecture on tubular constructs with 1 mm allowed for aligned ECM deposition and consequent impressive compliance using PCL, a rather stiff thermoplastic material, as scaffolding material. It is important to mention, that future improvement of the MEW process is required to generate tubular scaffolds with tunable mechanical properties and internal diameters below 1 mm diameter. Recent works have reported the design and melt-electrowriting of auxetic tubular microfibers with unprecedented control of elastic deformations that could be applied in engineered kidney tubules. However, internal diameters obtained were one order of magnitude higher, 10 mm, than the ones reported here (Paxton et al., 2020).

Next Steps Toward Perfusable and Vascularized Engineered Kidney Tubules

As mentioned above, the establishment of long-term perfusion systems will further advance kidney tubule performance and readouts. Moreover, the flexible nature of MEW tubular scaffolds allows the intertwinement of multiple scaffolds, which would create direct contact between epithelium and endothelium, mimicking the physiological situation (Hironaka et al., 1993; van Genderen et al., 2018). Twisting scaffolds would additionally protect and stabilize the constructs. To engineer peritubular blood vessels, the initial pore size could be reduced by combination of MEW with electrospinning, as shown by Jungst et al. (2019) and Pennings et al. (2019). Furthermore, the use of supportive cell types like pericytes or fibroblasts could help in the formation of endothelial monolayers (Bertlein et al., 2018). In fact, direct contact between different cell types on PCL scaffolds, as opposed to indirect contact, can improve cell functionality (Wang et al., 2015). Also, co-cultures of endothelial cells with renal epithelial cells have been shown to stimulate the balanced expression of various endothelial factors, which in turn improved the performance of renal cells (Tasnim and Zink, 2012).

In conclusion, we report the fabrication of self-supportive and yet small-sized porous MEW tubular scaffolds for kidney tubule engineering. MEW scaffolds enable direct access to the basolateral and luminal cell sides to facilitate solute exchange with vasculature in immediate proximity, which is critical for functional proximal tubule constructs. We showed that rhombus-shaped pores can enhance kidney tubule performance through topographic guidance, highlighting the fact that proper scaffold design offers opportunities to improve cell function.

DATA AVAILABILITY STATEMENT

The datasets presented in this study can be found in online repositories. The names of the repository/repositories and accession number(s) can be found below: <https://doi.org/10.1101/2020.09.16.300004>.

AUTHOR CONTRIBUTIONS

AG, KJ, JJ, RM, and MC contributed to the conception of this research. AG, KJ, TV, JJ, RM, and MC contributed to the experimental setup. AG, KJ, MK, JD, YL, CS, and MC performed the experimental work and data analysis. AG, KJ, MK, RM, and MC wrote the content of the manuscript. All authors contributed to drafting and critically revising it and have read and approved the final submitted manuscript.

FUNDING

The Dutch Kidney Foundation (17PHD16) supported the work of AG. The Netherlands Organization for Scientific Research (NWO) as part of the Future Medicines Program (022.006.003) supported the work of KJ and CS. The authors are also grateful for the support of the Gravitation Program Materials Driven Regeneration by the Netherlands Organization for Scientific research (024.003.013).

ACKNOWLEDGMENTS

MC acknowledges the strategic alliance between University Medical Center Utrecht and Technical University Eindhoven. MC, JM, TV, and RM acknowledge the partners of Regenerative Medicine Crossing Borders (www.regmedxb.com), powered by Health~Holland, Top Sector Life Sciences & Health.

SUPPLEMENTARY MATERIAL

The Supplementary Material for this article can be found online at: <https://www.frontiersin.org/articles/10.3389/fbioe.2020.617364/full#supplementary-material>

Supplementary Figure 1 | (A) Schematic of the melt electrowriting set-up, showing the collection of thin electrified polymer jets onto a computer controlled, rotating and translating mandrel. **(B)** Representation of the mandrel velocities, translational (V_{trans}), tangential (V_{tang}), rotational (V_{rot}), as well as winding angle (α), coil angle (\ominus), tube length, pitch and mandrel perimeter (r) in the mandrel surface during fiber collection. Winding angle was engineered by the ratio between V_{tang} and V_{trans} at constant fiber length.

Supplementary Figure 2 | Comparison between designed and printed winding angle for constructs with 1, 5, and 10 stacked layers and mandrel with **(A)** 0.5 mm and **(B)** 3 mm in diameter.

Supplementary Figure 3 | (A) Tensile tester set up and **(B)** representative engineered stress-strain curves with determined mechanical parameters for tubular scaffolds with rhombus and random microarchitecture with cells.

Supplementary Figure 4 | Custom made perfusion system used for renal barrier function studies. MEW tubular scaffolds were mounted in a 3D printed PLA customized chamber and then perfused.

Supplementary Table 1 | Water contact angles on uncoated PCL and L-DOPA coated PCL surfaces. Mean \pm SEM, $n = 3$.

Supplementary Movie 1 | Video for melt-electrowriting of tubular constructs with rhombus microstructure.

Supplementary Movie 2 | Perfusion of engineered tubules for renal barrier function testing.

REFERENCES

- Andalib, M. N., Dzenis, Y., Donahue, H. J., and Lim, J. Y. (2016). Biomimetic substrate control of cellular mechanotransduction. *Biomater. Res.* 20:11. doi: 10.1186/s40824-016-0059-1
- Bertlein, S., Hikimoto, D., Hochleitner, G., Hummer, J., Jungst, T., Matsusaki, M., et al. (2018). Development of endothelial cell networks in 3D tissues by combination of melt electrospinning writing with cell-accumulation technology. *Small*. 14. doi: 10.1002/smll.201701521
- Bourget, J.-M., Germain, L., Guillemette, M., and Veres, T. (2013). *Alignment of Cells and Extracellular Matrix Within Tissue-Engineered Substitutes*. doi: 10.5772/54142
- Brennan, C. M., Eichholz, K. F., and Hoey, D. A. (2019). The effect of pore size within fibrous scaffolds fabricated using melt electrospinning on human bone marrow stem cell osteogenesis. *Biomed. Mater.* 14:065016. doi: 10.1088/1748-605X/ab49f2
- Brown, T. D., Dalton, P. D., and Huttmacher, D. W. (2011). Direct writing by way of melt electrospinning. *Adv. Mater.* 23, 5651–5657. doi: 10.1002/adma.201103482
- Brown, T. D., Edin, F., Detta, N., Skelton, A. D., Huttmacher, D. W., and Dalton, P. D. (2014). Melt electrospinning of poly(epsilon-caprolactone) scaffolds: phenomenological observations associated with collection and direct writing. *Mater. Sci. Eng. C Mater. Biol. Appl.* 45, 698–708. doi: 10.1016/j.msec.2014.07.034
- Caetano-Pinto, P., Janssen, M. J., Gijzen, L., Verscheijden, L., Wilmer, M. J., and Masereeuw, R. (2016). Fluorescence-based transport assays revisited in a human renal proximal tubule cell line. *Mol. Pharm.* 13, 933–944. doi: 10.1021/acs.molpharmaceut.5b00821
- Castilho, M., Feyen, D., Flandes-Iparraguirre, M., Hochleitner, G., Groll, J., Doevendans, P. A. F., et al. (2017). Melt electrospinning writing of poly-hydroxymethylglycolide-co-epsilon-caprolactone-based scaffolds for cardiac tissue engineering. *Adv. Healthc. Mater.* 6. doi: 10.1002/adhm.201700311
- Castilho, M., Mouser, V., Chen, M., Malda, J., and Ito, K. (2019). Bi-layered micro-fibre reinforced hydrogels for articular cartilage regeneration. *Acta Biomater.* 95, 297–306. doi: 10.1016/j.actbio.2019.06.030
- Castilho, M., van Mil, A., Maher, M., Metz, C. H. G., Hochleitner, G., Groll, J., et al. (2018). Melt electrospinning allows tailored microstructural and mechanical design of scaffolds to advance functional human myocardial tissue formation. *Adv. Funct. Mater.* 28. doi: 10.1002/adfm.201803151
- Chambard, M., Gabrion, J., and Mauchamp, J. (1981). Influence of collagen gel on the orientation of epithelial cell polarity: follicle formation from isolated thyroid cells and from preformed monolayers. *J Cell Biol.* 91, 157–166. doi: 10.1083/jcb.91.1.157
- Duclos, G., Garcia, S., Yevick, H. G., and Silberzan, P. (2014). Perfect nematic order in confined monolayers of spindle-shaped cells. *Soft Matter*. 10, 2346–2353. doi: 10.1039/C3SM52323C
- Eichholz, K. F., and Hoey, D. A. (2018). Mediating human stem cell behaviour via defined fibrous architectures by melt electrospinning writing. *Acta Biomater.* 75, 140–151. doi: 10.1016/j.actbio.2018.05.048
- Frohlich, E. M., Alonso, J. L., Borenstein, J. T., Zhang, X., Arnaout, M. A., and Charest, J. L. (2013). Topographically-patterned porous membranes in a microfluidic device as an *in vitro* model of renal reabsorptive barriers. *Lab Chip* 13, 2311–2319. doi: 10.1039/c3lc50199j
- Frohlich, E. M., Zhang, X., and Charest, J. L. (2012). The use of controlled surface topography and flow-induced shear stress to influence renal epithelial cell function. *Integr. Biol.* 4, 75–83. doi: 10.1039/C1IB00096A
- Gasiorowski, J. Z., Liliensiek, S. J., Russell, P., Stephan, D. A., Nealey, P. F., and Murphy, C. J. (2010). Alterations in gene expression of human vascular endothelial cells associated with nanotopographic cues. *Biomaterials* 31, 8882–8888. doi: 10.1016/j.biomaterials.2010.08.026
- Hironaka, K., Makino, H., Yamasaki, Y., and Ota, Z. (1993). Renal basement membranes by ultrahigh resolution scanning electron microscopy. *Kidney Int.* 43, 334–345. doi: 10.1038/ki.1993.51
- Homan, K. A., Kolesky, D. B., Skylar-Scott, M. A., Herrmann, J., Obuobi, H., Moisan, A., et al. (2016). Bioprinting of 3D convoluted renal proximal tubules on perfusable chips. *Sci. Rep.* 6:34845. doi: 10.1038/srep34845
- Hulshof, F., Schophuizen, C., Mihajlovic, M., van Blitterswijk, C., Masereeuw, R., de Boer, J., et al. (2018). New insights into the effects of biomaterial chemistry and topography on the morphology of kidney epithelial cells. *J. Tissue Eng. Regen. Med.* 12, e817–e27. doi: 10.1002/term.2387
- Jang, K. J., Mehr, A. P., Hamilton, G. A., McPartlin, L. A., Chung, S., Suh, K. Y., et al. (2013). Human kidney proximal tubule-on-a-chip for drug transport and nephrotoxicity assessment. *Integr. Biol.* 5, 1119–1129. doi: 10.1039/c3ib40049b
- Jansen, J., De Napoli, I. E., Fedecostante, M., Schophuizen, C. M., Chevchik, N. V., Wilmer, M. J., et al. (2015). Human proximal tubule epithelial cells cultured on hollow fibers: living membranes that actively transport organic cations. *Sci. Rep.* 5:16702. doi: 10.1038/srep16702
- Jansen, J., Fedecostante, M., Wilmer, M. J., Peters, J. G., Kreuser, U. M., van den Broek, P. H., et al. (2016). Bioengineered kidney tubules efficiently excrete uremic toxins. *Sci. Rep.* 6:26715. doi: 10.1038/srep26715
- Jansen, J., Schophuizen, C. M., Wilmer, M. J., Lahham, S. H., Mutsaers, H. A., Wetzels, J. F., et al. (2014). A morphological and functional comparison of proximal tubule cell lines established from human urine and kidney tissue. *Exp. Cell Res.* 323, 87–99. doi: 10.1016/j.yexcr.2014.02.011
- Jansen, K., Castilho, M., Aarts, S., Kaminski, M. M., Lienkamp, S. S., Pichler, R., et al. (2019). Fabrication of kidney proximal tubule grafts using biofunctionalized electrospun polymer scaffolds. *Macromol. Biosci.* 19:e1800412. doi: 10.1002/mabi.201800412
- Jansen, K., Schuurmans, CCL, Jansen, J., Masereeuw, R., and Vermonden, T. (2017). Hydrogel-based cell therapies for kidney regeneration: current trends in biofabrication and *in vivo* repair. *Curr. Pharm. Des.* 23, 3845–3857. doi: 10.2174/1381612823666170710155726
- Joly, P., Duda, G. N., Schone, M., Welzel, P. B., Freudenberg, U., Werner, C., et al. (2013). Geometry-driven cell organization determines tissue growths in scaffold pores: consequences for fibronectin organization. *PLoS ONE*. 8:e73545. doi: 10.1371/journal.pone.0073545
- Jungst, T., Pennings, I., Schmitz, M., Rosenberg, AJWP, Groll, J., and Gawlitza, D. (2019). Heterotypic scaffold design orchestrates primary cell organization and phenotypes in cocultured small diameter vascular grafts. *Adv. Funct. Mater.* 29. doi: 10.1002/adfm.201905987
- Kennedy, K. M., Bhaw-Luximon, A., and Jhurry, D. (2017). Cell-matrix mechanical interaction in electrospun polymeric scaffolds for tissue engineering: Implications for scaffold design and performance. *Acta Biomater.* 50, 41–55. doi: 10.1016/j.actbio.2016.12.034
- Kim, S. O., Kim, J., Okajima, T., and Cho, N. J. (2017). Mechanical properties of paraformaldehyde-treated individual cells investigated by atomic force microscopy and scanning ion conductance microscopy. *Nano Conver.* 4:5. doi: 10.1186/s40580-017-0099-9
- Li, X., Balagam, R., He, T. F., Lee, P. P., Igoshin, O. A., and Levine, H. (2017). On the mechanism of long-range orientational order of fibroblasts. *Proc. Natl. Acad. Sci. U. S. A.* 114, 8974–8979. doi: 10.1073/pnas.1707210114
- Lin, NYC, Homan, K. A., Robinson, S. S., Kolesky, D. B., Duarte, N., Moisan, A., et al. (2019). Renal reabsorption in 3D vascularized proximal tubule models. *Proc. Natl. Acad. Sci. U. S. A.* 116, 5399–5404. doi: 10.1073/pnas.1815208116
- Ling, Y., Li, C., Feng, K., Duncan, R., Eisma, R., Huang, Z., et al. (2016). Effects of fixation and preservation on tissue elastic properties measured by quantitative optical coherence elastography (OCE). *J. Biomech.* 49, 1009–1015. doi: 10.1016/j.jbiomech.2016.02.013
- McCull, E., Groll, J., Jungst, T., and Dalton, P. D. (2018). Design and fabrication of melt electrospun tubes using intuitive software. *Mater. Design.* 155, 46–58. doi: 10.1016/j.matdes.2018.05.036
- Ni, M., Teo, J. C., Ibrahim, M. S., Zhang, K., Tasnim, F., Chow, P. Y., et al. (2011). Characterization of membrane materials and membrane coatings for bioreactor units of bioartificial kidneys. *Biomaterials* 32, 1465–1476. doi: 10.1016/j.biomaterials.2010.10.061
- Oo, Z. Y., Deng, R., Hu, M., Ni, M., Kandasamy, K., bin Ibrahim, M. S., et al. (2011). The performance of primary human renal cells in hollow fiber bioreactors for bioartificial kidneys. *Biomaterials* 32, 8806–8815. doi: 10.1016/j.biomaterials.2011.08.030
- Paxton, N. C., Daley, R., Forrestal, D. P., Allenby, M. C., and Woodruff, M. A. (2020). Auxetic tubular scaffolds via melt electrospinning. *Mater. Des.* 193:108787. doi: 10.1016/j.matdes.2020.108787
- Pennings, I., van Haften, E. E., Jungst, T., Bulsink, J. A., Rosenberg, A., Groll, J., et al. (2019). Layer-specific cell differentiation in bi-layered vascular grafts under flow perfusion. *Biofabrication* 12:015009. doi: 10.1088/1758-5090/ab47f0
- Privratsky, J. R., and Newman, P. J. (2014). PECAM-1: regulator of endothelial junctional integrity. *Cell Tissue Res.* 355, 607–619. doi: 10.1007/s00441-013-1779-3

- RayChaudhury, A., Elkins, M., Kozien, D., and Nakada, M. T. (2001). Regulation of PECAM-1 in endothelial cells during cell growth and migration. *Exp. Biol. Med.* 226, 686–691. doi: 10.1177/153537020222600715
- Rayner, S. G., Phong, K. T., Xue, J., Lih, D., Shankland, S. J., Kelly, E. J., et al. (2018). Reconstructing the human renal vascular-tubular unit *in vitro*. *Adv. Healthc. Mater.* 7:e1801120. doi: 10.1002/adhm.201801120
- Robinson, T. M., Hutmacher, D. W., and Dalton, P. D. (2019). The next frontier in melt electrospinning: taming the jet. *Adv. Funct. Mater.* 29. doi: 10.1002/adfm.201904664
- Saidy, N. T., Wolf, F., Bas, O., Keijndener, H., Hutmacher, D. W., Mela, P., et al. (2019). Biologically inspired scaffolds for heart valve tissue engineering via melt electrowriting. *Small* 15:e1900873. doi: 10.1002/smll.201900873
- Sankaran, J., Uzer, G., van Wijnen, A. J., and Rubin, J. (2019). Gene regulation through dynamic actin control of nuclear structure. *Exp. Biol. Med.* 244, 1345–1353. doi: 10.1177/1535370219850079
- Singh, N. K., Han, W., Nam, S. A., Kim, J. W., Kim, J. Y., Kim, Y. K., et al. (2020). Three-dimensional cell-printing of advanced renal tubular tissue analogue. *Biomaterials* 232:119734. doi: 10.1016/j.biomaterials.2019.119734
- Tasnim, F., and Zink, D. (2012). Cross talk between primary human renal tubular cells and endothelial cells in cocultures. *Am. J. Physiol. Renal Physiol.* 302, F1055–F1062. doi: 10.1152/ajprenal.00621.2011
- Tremblay, D., Andrzejewski, L., Leclerc, A., and Pelling, A. E. (2013). Actin and microtubules play distinct roles in governing the anisotropic deformation of cell nuclei in response to substrate strain. *Cytoskeleton* 70, 837–848. doi: 10.1002/cm.21148
- Tylek, T., Blum, C., Hrynevich, A., Schlegelmilch, K., Schilling, T., Dalton, P. D., et al. (2020). Precisely defined fiber scaffolds with 40 μm porosity induce elongation driven M2-like polarization of human macrophages. *Biofabrication* 12:025007. doi: 10.1088/1758-5090/ab5f4e
- van Genderen, A. M., Jansen, J., Cheng, C., Vermonden, T., and Masereeuw, R. (2018). Renal tubular- and vascular basement membranes and their mimicry in engineering vascularized kidney tubules. *Adv. Healthc. Mater.* 7:e1800529. doi: 10.1002/adhm.201800529
- Vriend, J., Peters, JGP, Nieskens, TTG, Skovronova, R., Blaimschein, N., Schmidts, M., et al. (2020). Flow stimulates drug transport in a human kidney proximal tubule-on-a-chip independent of primary cilia. *Biochim. Biophys. Acta Gen. Subj.* 1864:129433. doi: 10.1016/j.bbagen.2019.129433
- Wang, Z., Teoh, S. H., Hong, M., Luo, F., Teo, E. Y., Chan, J. K., et al. (2015). Dual-microstructured porous, anisotropic film for biomimicking of endothelial basement membrane. *ACS Appl. Mater. Interfaces* 7, 13445–13456. doi: 10.1021/acsami.5b02464
- Weber, E. J., Chapron, A., Chapron, B. D., Voellinger, J. L., Lidberg, K. A., Yeung, C. K., et al. (2016). Development of a microphysiological model of human kidney proximal tubule function. *Kidney Int.* 90, 627–637. doi: 10.1016/j.kint.2016.06.011

Conflict of Interest: The authors declare that the research was conducted in the absence of any commercial or financial relationships that could be construed as a potential conflict of interest.

Copyright © 2021 van Genderen, Jansen, Kristen, van Duijn, Li, Schuurmans, Malda, Vermonden, Jansen, Masereeuw and Castilho. This is an open-access article distributed under the terms of the Creative Commons Attribution License (CC BY). The use, distribution or reproduction in other forums is permitted, provided the original author(s) and the copyright owner(s) are credited and that the original publication in this journal is cited, in accordance with accepted academic practice. No use, distribution or reproduction is permitted which does not comply with these terms.